Numerical investigation of the turbulence characteristics and energy dissipation mechanism of baffle drop shafts

Qinghua Yang and Qian Yang

ABSTRACT

The baffle drop shaft is widely used in deep tunnel drainage systems due to its fine applicability and high energy dissipation. To fully study the turbulence characteristics and energy dissipation mechanism of baffle drop shafts, a 1:25 scale physical model test and a numerical simulation based on the Realizable k-ϵ model and Volume of Fluid (VOF) method were performed. The results showed that a baffle spacing that is too dense or too sparse is not conducive to energy dissipation and discharge. The minimum baffle spacing is the optimal structural design at the design flow rate when the flow regime is free-drop flow. The energy dissipation calculation model established in this paper has high accuracy for calculating the energy dissipation rate on the baffles in free-drop flow. The energy dissipation modes of the shaft can be divided into inlet energy dissipation, baffle energy dissipation, and shaft-bottom energy dissipation. Baffles play a major role in the energy dissipation at low flow rates, and the proportions of inlet and shaft-bottom energy dissipation increase with the increase in flow rate.

Key words | baffle drop shaft, energy dissipation calculation model, energy dissipation mechanism, energy dissipation rate, hydraulic model test, numerical simulation

Qinghua Yang
Qian Yang (corresponding author)
School of Civil Engineering,
Southwest Jiaotong University,
Chengdu 610031,
China
E-mail: *yangqian-swjtu@foxmail.com*

HIGHLIGHTS

- The calculation model of baffle energy dissipation has a better ability to predict the energy dissipation rate of the baffle drop shaft in the free-drop flow regime.
- This paper elaborates on the energy dissipation mechanism of the baffle drop shaft through energy dissipation type and energy dissipation mode, which can provide help for in-depth analysis of the energy dissipation characteristics of baffle drop shafts.

INTRODUCTION

Since the construction of the 'sponge city' was proposed by the Chinese government in 2013, the deep tunnel drainage system has gradually become the main way for big cities to solve flood disasters and overflow pollution in old urban areas (Liu *et al.* 2017). At present, the planning and construction of deep tunnels have been carried out in China, such as Beijing, Shanghai, Guangzhou, Shenzhen, Chengdu and other cities (Wu *et al.* 2016). As an important part of a deep tunnel drainage system, the drop shaft is used to transport the rainwater and sewage from the shallow drainage network to the deep tunnel. There are four types of drop shafts, including vertical drop shafts, vortex drop shafts, stepped drop shafts, and baffle drop shafts (Shen *et al.* 2019). In view of its good energy dissipation effect and its applicability for different inflows, the baffle drop shaft has been widely employed in deep tunnel drainage systems (Yang *et al.* 2020).

The design guides of the drop manhole are provided in the Design manual for the water supply and drainage

doi: 10.2166/wst.2021.137

(China Architecture & Building Press 2017), but the research on energy dissipation mainly focuses on the vertical drop shaft and vortex drop shaft. Using hydraulic experimentation, Granata *et al.* (2011) explored the influence of different downstream water heads on the energy dissipation in a drop manhole and established expressions for the energy loss. The provided relations are useful to improve the structural design of the drop manhole. An experimental investigation on the hydraulic characteristics inside stacked drop manholes was carried out by Camino *et al.* (2011), and the mechanism of energy dissipation with different flow regimes was analyzed. It was found that the total energy dissipation in the stacked manhole was 50% to 90%, and the contribution of each chamber to the overall energy dissipation was different under different inflow rates and flow regimes. Chanson (2007) pointed out that the water-gas two-phase flow characteristics of vertical drop shafts are extremely complex, and the energy dissipation rate of the shaft depended on the internal flow regimes. In addition, the energy dissipation characteristics of the vortex drop shaft were also the research focus for many scholars (Pfister *et al.* 2018; Mahmoudi-Rad & Khanjani 2019). Through a series of experimental data analysis, Crispino *et al.* (2019; 2021) found that the energy dissipation of vortex drop shafts was mainly concentrated in the dissipation chamber, and the energy dissipation efficiency was mostly related to the turbulence and flow impact occurring in the chamber. Through physical model test and numerical simulation, the hydraulic characteristics of a new type of vortex drop shaft were studied by Zhang *et al.* (2018). The results revealed that water flowing into the shaft could carry a large quantity of air and form a stable mixing cavity by changing the flow conditions and increasing the clearance height of the vortex chamber. However, the structural parameters including the slope section, vertical shaft and vortex chamber need to be optimized to determine the best shaft shape for stable and safe operation. Liu *et al.* (2018) designed a novel internal energy dissipation vortex shaft, and experimentally and numerically investigated the energy dissipation characteristics and movement mechanism of the new shaft. However, this kind of shaft is only suitable for hydraulic engineering due to the necessary conditions of stable water head and large inflow area during operation. In order to improve the security and energy dissipation, an innovative design structure named the helicoidal-stepped drop shaft was proposed by Qi *et al.* (2018). By using numerical simulations, the flow regime and hydraulic characteristic of the stepped drop shaft with different central angles were investigated, but the air entrainment characteristics and energy dissipation performance of stepped drop shafts need further research. In Liao *et al.* (2019), the energy dissipation rate, fluctuating pressure, and anti-cavitation performance of helicoidal-stepped drop shafts were experimentally investigated.

Presently, the research on the baffle drop shaft mainly focuses on the hydraulic characteristics and energy dissipation performance. A physical model test was carried out by Margevicius *et al.* (2010) to study the water-air two-phase flow characteristics in baffle drop shafts. By improving and optimizing the structural parameters of the shaft, air entrainment flowing into the main tunnel could be minimized at design discharges. However, the flow velocity distribution on different baffles is not clear due to the limitation of the test. Moreover, Odgaard *et al.* (2013) experimentally investigated the air entrainment characteristics in baffle drop shafts and provided a dimensionless relationship between the key parameters for structural design. But the angle of the baffle was not considered in this research. For the Southeast Collector (SEC) deep tunnel systems project in York, Ontario, Canada, two different types of drop shafts (plunge and baffle) physical model were constructed and tested. By comparing the discharge capacity, energy dissipation effect, and air entrainment, reasonable suggestions for this project were put forward by Stirrup *et al.* (2012). To increase the discharge capacity of the baffle drop shaft, many researchers have attempted to improve and optimize the shaft structure. A novel baffle drop shaft with no dry side was proposed by Wang *et al.* (2020), and the influences of the baffle spacing and flow rate on hydraulic characteristics of this shaft were numerically investigated.

Although the existing researches have gained a comprehensive understanding into the baffle drop shaft, little is known about the turbulence characteristics and energy dissipation mechanisms. In this paper, numerical simulations were performed to analyze the flow regimes and baffle functions, establish expressions for the energy dissipation on the baffles, and explore the energy dissipation mechanism in baffle drop shafts.

EXPERIMENTAL SETUP

As shown in Figure 1, the deep tunnel drainage system considered in this study was mainly composed of an inlet pipe, drop shaft, outlet pipe, and drainage main tunnel. The drop shaft was divided into a wet side and dry side by a dividing wall. The side with the baffles was the wet side for discharge

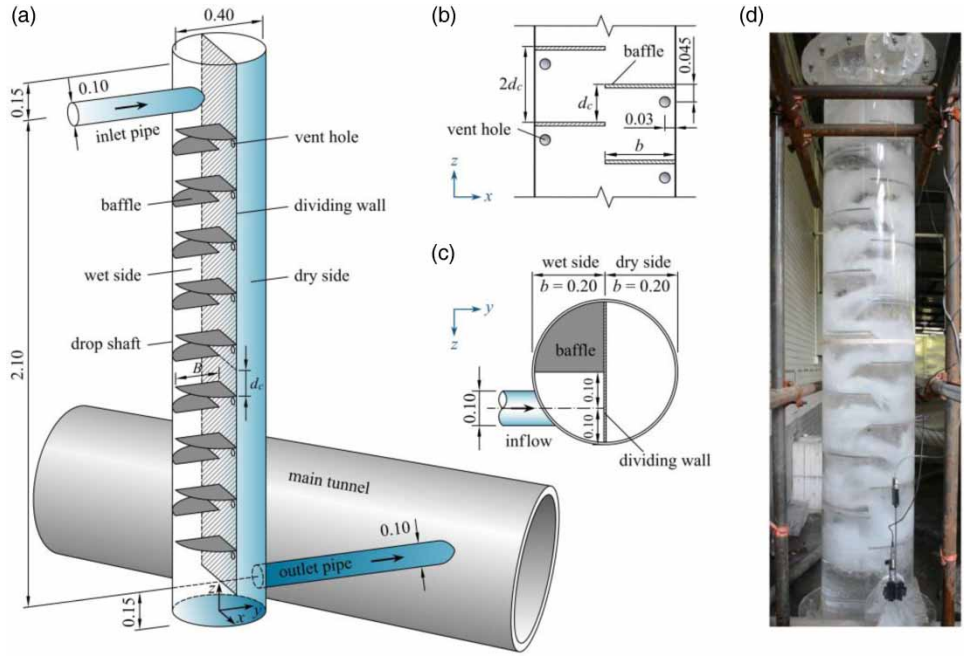

Figure 1 | Sketch of experimental setup: (a) deep tunnel drainage system; (b) vertical view of the drop shaft (partial); (c) top view of the drop shaft; (d) Plexiglass model (unit: meter).

and energy dissipation, and the other side was the dry side for aeration. Based on the typical cases of deep tunnel drainage systems in China and abroad, the buried depths of the main tunnels are 40–100 m, and the drop shaft length was designed to be 60 m in this paper. Combined with the structural characteristics and test site conditions, the physical model of the baffle drop shaft was designed at a scale of 1:25 based on Froude similitude.

To observe the flow regimes and measure the hydraulic parameters, the physical model of the baffle drop shaft was made of transparent plexiglass (Figure 1(d)). The height of the drop shaft was $H = 2.4$ m, and the diameter of the shaft was 0.4 m. The top of the drop shaft was connected to the atmosphere. The diameters of the inlet and outlet pipes were 0.1 m, and the heights of the central axes of the inlet and outlet pipes from the bottom of the shaft were 2.25 and 0.15 m, respectively. The central angle of the fan-shaped baffle was 90°, and the model width of the baffle edge (b) was 0.2 m. The baffle was arranged horizontally, and the spacings (d_c) between adjacent baffles could be adjusted to 0.0802, 0.097, and 0.1228 m depending on the experimental requirements. The distance from the first baffle to the central axis of the inlet pipe was 0.12 m. Vent holes with diameters of 0.03 m were arranged on the dividing wall below each baffle, and the distances between the center of the vent hole and the upper baffle and between the center of the vent hole and the shaft wall were 0.03 and 0.045 m, respectively.

A data acquisition system named SDA1000-SW-V02 was used in the tests to achieve synchronous real-time collection. The cross-section average flow velocities of the inlet and outlet pipes were measured by a propeller velocimeter with a measurement range of 0.01–4 m/s and an accuracy of ±1.5%. The flow rate of the drop shaft was measured using an electromagnetic flow meter with a full-scale accuracy of ±0.5%. In addition, the flow rates were controlled by a valve. The range of the flow rates (Q) in this test was 4.2–14.0 L/s, and the dimensionless flow rate (Q^*) was calculated as follows:

$$Q^* = Q/\sqrt{gb^5} \tag{1}$$

where Q (m^3/s) is the flow rate, b (m) is the model width of the baffle edge, and g (m/s^2) is the acceleration of gravity.

To clearly observe the variations of the flow regime when the shaft was in operation, a Nikon® D850 high-speed camera with a pixel resolution of 48 million and a frame rate of 60 Hz was used. All tests were carried out under steady flow conditions, and the eight groups of dimensionless flow rates and three groups of baffle spacings are shown in Table 1. To facilitate the comparison with the numerical results, the measured values of the physical tests were converted into prototype values.

Table 1 | Summary of the operating conditions for the simulations and tests

b (m)	d_c (m)	d_p (m)	$d^* = d_p/B$	Total number of baffles	Case	Q^*
0.20	–	1.84	0.368	26	Simulation 1	0.075; 0.100
	0.0802	2.01	0.401	24	Test 1 and simulation 2	0.125; 0.150
	0.0970	2.43	0.485	20	Test 2 and simulation 3	0.175; 0.200
	0.1228	3.07	0.614	16	Test 3 and simulation 4	0.225; 0.250
	–	3.54	0.708	13	Simulation 5	(All cases were carried out under these 8 groups of Q^*)
	–	4.19	0.838	11	Simulation 6	

NUMERICAL SIMULATION

In this study, the computational fluid dynamics module of the ANSYS Fluent 16.0 software (ANSYS®, Canonsburg, PA, USA) (Canonsburg 2015), was used to simulate the turbulence characteristics of the baffle drop shaft at different flow rates.

CFD model

Compared with the renormalization group (RNG) k-ε model and the standard k-ε model, the realizable k-ε model can predict the divergence of the baffle jet and calculate complex flows, such as the rotational shear flow and free flow, more accurately (Zhang *et al.* 2011; Gildeh *et al.* 2014; Mohsin & Kaushal 2016; Hnaien *et al.* 2018). Therefore, the realizable k-ε model was used in this study. The flow characteristics in the baffle drop shaft were complex, and the mixing degree of the water and air was extremely high. Therefore, the volume of fluid (VOF) method was used to track the free surface of the high-speed water flow.

Grid generation and boundary conditions

The prototype geometric model of the baffle drop shaft was created by the Autodesk Revit software based on the physical model and length scales. The pre-processing software ICEM CFD was used to create the calculation area and divide the grid. Considering the structural characteristics of a baffle drop shaft with a complex curve, the unstructured grid generation method was used to discretize the three-dimensional calculation area. In the numerical model, three kinds of prototype baffle spacings (d_p) were added as supplementary research, and d_p was 1.84, 2.01, 2.43, 3.07, 3.54, and 4.19 m. The prototype width of the baffle edge was $B = 5$ m. The operating conditions for the simulation are shown in Table 1.

The grid density had a direct impact on the calculation results and convergence stability. If the grid was too dense, the number of calculations would increase. However, if the grid was too sparse, the convergence stability would decrease, and the calculation error would increase. Therefore, it was important to determine a reasonable grid density. In this paper, the relative error of the outlet velocity was selected for the grid independence test when $Q^* = 0.150$ and $d^* = 0.485$. In addition, Jiao & Deng (2013) proposed that the results were reliable if the error of the calculation results obtained by different grid numbers was within 2%, using the Fluent software. The relative errors χ and ξ can be calculated as follows:

$$\chi = |v_m - v_s|/v_m \times 100\% \tag{2}$$

$$\xi = |v_{s,\max} - v_s|/v_{s,\max} \times 100\% \tag{3}$$

where χ is the relative error of the measured velocity, ξ is relative error of the simulated velocity, v_m is the measured outlet velocity, v_s is the simulated outlet velocity, and $v_{s,\max}$ is the simulated outlet velocity when the number of grid elements was 2.45 million.

Figure 2 shows the test results of the grid dependence analysis. The velocity change rate χ and ξ met the qualified standard of 2% when the grid number (n) was more than

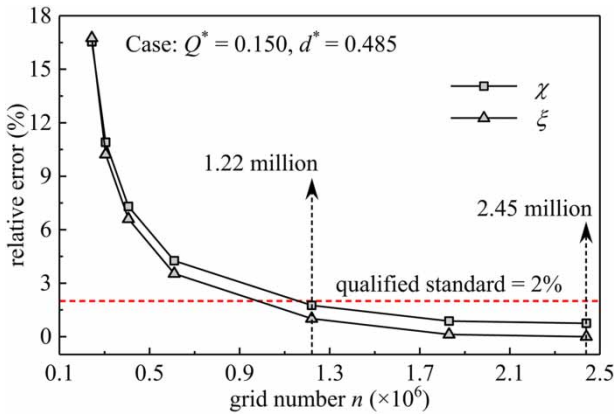

Figure 2 | Test results of grid independence.

1.22 million. Considering the computational accuracy and efficiency, the grid number of 1.22 million was adopted for the following calculations, and the grid size was between 0.05 and 0.20 m. The local grid of the baffle drop shaft is shown in Figure 3.

A velocity inlet boundary was used for the water inlet, and the value of the average velocity was obtained based on the flow continuity equation and flow rate. A free flow boundary was adopted as the water outlet. The free surface of water was assumed to be a pressure inlet, and the value of the pressure was 0. The drop shaft wall and baffle wall were defined as no-slip wall boundaries, and the non-equilibrium wall function method was used to analyze the near-wall regions of the flow.

RESULT VALIDATION AND ANALYSIS

Model verification

The outlet velocity was selected to verify the accuracy of the model. The formula for the relative error of the outlet velocity is defined as:

$$\delta = |v_{o,m} - v_{o,s}|/v_{o,m} \times 100\% \quad (4)$$

where δ is relative error of the outlet velocity at different flow rates, $v_{o,m}$ is the measured outlet velocity at different flow rates, and $v_{o,s}$ is the simulated outlet velocity at different flow rates.

The comparison of the outlet velocities of the tests and numerical simulations is shown in Figure 4. The relative error range was 0.2–6.7%, and the numerical results showed good agreement with the test measurements. Therefore, this numerical simulation method could be used to describe the hydraulic behaviors of the baffle drop shaft, and the accuracy of the calculation results was high.

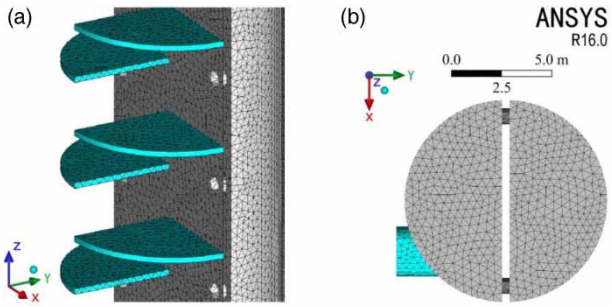

Figure 3 | Schematic diagram of local grid: (a) grid of baffles and shaft wall (grid of shaft wall at wet side is not shown) and (b) grid at the top of the drop shaft.

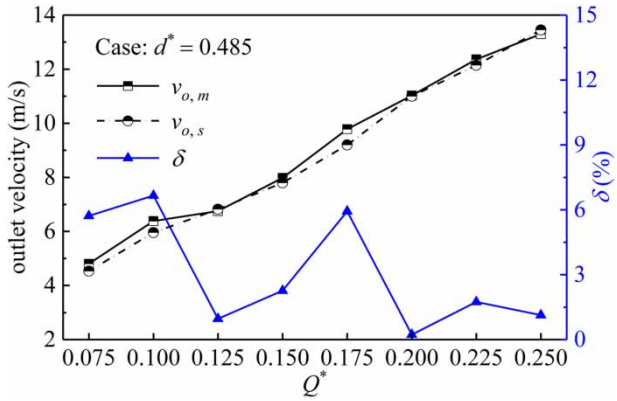

Figure 4 | Comparison of the outlet velocities.

Free surface and flow regimes

According to experimental observation, the water flow entering the shaft collided with the dividing wall and then fell to the first baffle immediately. Part of the water flow on the baffle subsequently jetted into the lower baffle from the baffle edge, and the other portion of the water flow formed an impact wave between the shaft wall and water jet (Figure 5(f)). The water flow then moved to the bottom of the shaft in the same flow state and collided with the shaft bottom. Part of the water flowed out of the outlet pipe, and the rest formed a water cushion at the shaft bottom. The inflow from the upper baffle collided and mixed with the water cushion, and the rolling water flow led to significant air bubble entrainment. The water flow at the shaft bottom was fully aerated and accompanied by energy dissipation. The flow characteristics, including the different flow regimes and cavity area phenomenon, were described in detail by Yang & Yang (2020), and these will not be explored in this paper. The numerical simulation results will be the focus of the study. Figure 5 shows a comparison of the flow regimes at the same position of the baffles between the physical model test and numerical simulation under different flow rates when $d^* = 0.401$. The calculated free surface and flow regimes on the baffles were fairly consistent with the test results. The results of Figure 5 again confirm the accuracy and reliability of the numerical simulations.

Turbulent kinetic energy distribution

The discharge process in the baffle drop shaft was typical turbulent motion, and the turbulence intensity could be expressed by the turbulent kinetic energy (k), defined as

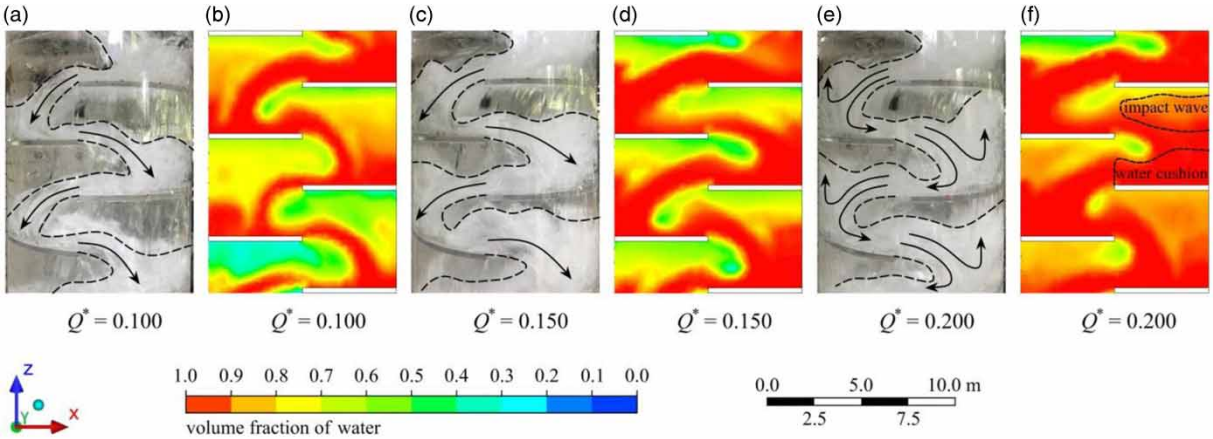

Figure 5 | Comparison of flow regimes on the baffles between the physical model test and numerical simulation under different flow rates: (a), (b) free-drop flow, (c), (d) critical flow, and (e), (f) wall-impact confined flow.

follows:

$$k = \frac{1}{2}(u'^2 + v'^2 + w'^2) \tag{5}$$

where u', v', and w' are the velocity components in x, y, and z directions, respectively.

As a physical quantity to express the turbulence intensity of the flow, the turbulent kinetic energy reflects the development and dissipation ability of the turbulence. The larger the turbulent kinetic energy, the stronger the turbulent flow in the shaft, and the greater the mixing and breakup degree of the water can be, and thus the energy dissipation effect of the shaft can be more prominent and vice versa. Figure 6 shows the cloud diagrams of the turbulent kinetic energy distribution with different baffle spacings at $Q^* = 0.150$. The distribution of the turbulent kinetic energy in the drop shaft was small at the central baffles and large at the upper and lower baffles when $d^* \leq 0.401$. In particular, the turbulent kinetic energy at the central baffle was less than 3×10^3 m^2/s^2. When $d^* \geq 0.485$, the turbulent kinetic energy was evenly distributed in the shaft, and with the increase in the baffle spacing, the distribution of the turbulent kinetic energy on the baffle became more evenly distributed. Comparing the flow regimes under the same test conditions, the flow on the baffle was wall-impact confined flow at $d^* = 0.401$, and free-drop flow appeared when $d^* = 0.485$ and 0.614. This result shows that the free-drop flow regime can make the turbulent kinetic energy distribution more evenly distributed and increase the energy loss.

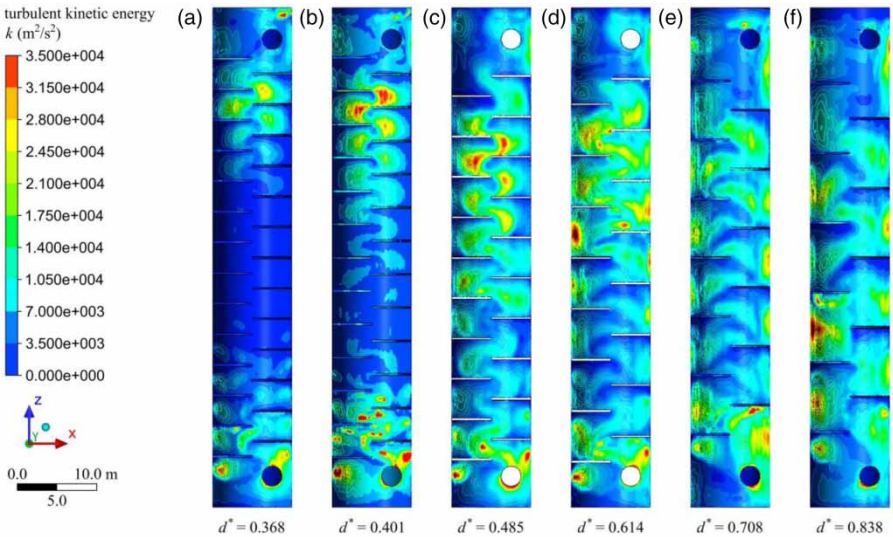

Figure 6 | Cloud diagrams of the turbulent kinetic energy distribution.

In summary, the size and distribution of the turbulent kinetic energy were affected by factors such as the flow rate and baffle spacing. The energy dissipation capability of the water on the baffles can be obtained by analyzing the variations of the turbulent kinetic energy in the shaft. In addition, the hydrodynamic load on the baffles will increase with the increase in the baffle spacing (Yang & Yang 2020). This will have a substantial impact on the safety of the shaft structure. Accordingly, the structural design of the baffle drop shaft should be carried out under the design flow rate conditions, the baffle spacing should be at a minimum when the flow regime in the shaft is free-drop flow. With this configuration, the discharge capacity and energy dissipation effect of the baffle drop shaft are optimal.

Turbulent dissipation rate distribution

According to the two-equation turbulence model, the turbulent dissipation rate (ε) is defined as follows:

$$\varepsilon = \frac{\mu}{\rho}\left(\frac{\partial u'_i}{\partial x_j}\frac{\partial u'_j}{\partial x_i}\right) \tag{6}$$

where $\partial u_i'/\partial x_j$ is the time-change rate of the time-averaged velocity (u_i') in the x_j direction, and $\partial u_j'/\partial x_i$ is the time-change rate of the time-averaged velocity (u_j') in the x_i direction.

Physically, the turbulent dissipation rate is the rate at which the turbulent kinetic energy is converted into the molecular thermal kinetic energy through the intermolecular viscosity of water; that is, the dissipation of turbulent kinetic energy per unit of time. The larger the turbulent dissipation rate, the faster the conversion rate of the thermal energy of water. Figure 7 shows the cloud diagrams of the turbulent dissipation rate distribution at different flow rates when $d^* = 0.614$. As shown by Figures 6(d) and 7(d), the distributions of the turbulent kinetic energy k and turbulent dissipation rate ϵ were similar under the same conditions. The influence of the flow rate on the turbulent dissipation rate will be discussed below.

As shown in Figure 7, $z = 8$–27 m and $z = 27$–49 m were defined as the middle-lower and upper-middle areas of the shaft, respectively, where z is the elevation from the bottom of the shaft. Figure 7(a)–7(h) show that the turbulent dissipation rate in the upper-middle area was larger than that in the middle-lower area of the shaft. This indicates that the turbulence intensity of the flow in the upper-middle area was more intense, and the dissipation of turbulent kinetic energy was greater. In addition, local increase occurred at the bottom of the shaft, because the orifice outflow increased the turbulent characteristic of the flow. A comparison of the variations of the turbulent dissipation rate at different flow rates revealed that the turbulent dissipation rate increased with the increase in the flow rate, and the local maximum turbulent dissipation rate on the same baffle gradually moved from the shaft wall to the baffle edge. When the flow rate was low, the water fell freely on the baffles. Due to the presence of the shaft wall, the flow boundary could not expand outward, and water flow rubbed against and collided with the shaft wall constantly. Therefore, a local maximum turbulent dissipation rate formed near the shaft wall. With the increase in the flow rate, the flow regime gradually changed from free-drop flow to wall-impact confined flow. A stable water cushion

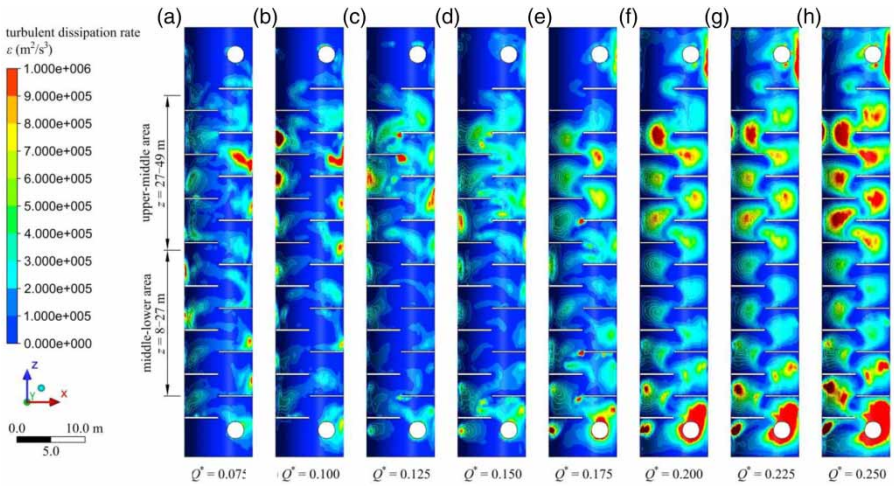

Figure 7 | Cloud diagrams of the turbulent dissipation rate distribution at different flow rates.

formed near the shaft wall at large flow rates. The relative motion between the water cushion and the shaft wall was weak. Thus, the turbulent dissipation rate was very low at the shaft wall. However, the water flow from the upper baffle collided with the water cushion violently, which increased the conversion rate of turbulent kinetic energy to thermal energy, and formed a local maximum here.

Calculation model of baffle energy dissipation

The energy dissipation of the baffle drop shaft can be regarded as the result of the superposition of multiple energy dissipation points, and the energy dissipation between the baffles is the main component of the shaft energy dissipation. The results presented above show that the flow regime on the baffle has a great influence on the energy dissipation of the shaft. Under the free-drop flow regime, the turbulent kinetic energy was uniformly distributed in the shaft, and the energy dissipation effect was very good. Therefore, the calculation model of the baffle energy dissipation was established based on free-drop flow in this study. Figure 8 shows the schematic diagram of the baffle energy dissipation calculation model. In this figure, h_1 and h_2 are the average flow depths at the second and third baffle edges, respectively, v_1 and v_2 are the average flow velocities at the second and third baffle edges, respectively, L_f is the horizontal distance from the baffle edge to the intersection of the streamline and baffle, B is the prototype width of the baffle edge. It was defined as free-drop flow when $L_f < B$ (Yang & Yang 2020).

Based on the experimental observations, after contacting the first baffle, the water fell to the second baffle in the free-drop flow regime and dropped baffle by baffle. Thus, the energy dissipation calculation of the drop shaft started from the second baffle. The energy loss ratio after the water falls to each baffle is denoted as λ. The specific energy of the second baffle (E_1) can be expressed as follows:

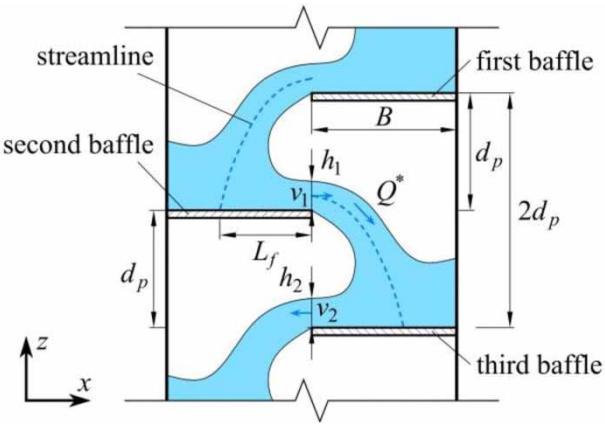

Figure 8 | Schematic diagram of baffle energy dissipation model.

$$E_1 = h_1 + \frac{v_1^2}{2g} \tag{7}$$

The residual energy of the third baffle is as follows:

$$E_2 = h_2 + \frac{v_2^2}{2g} = (1-\lambda)(E_1 + d_p) \tag{8}$$

By analogy, the residual energy of the nth ($n > 2$) baffle is as follows:

$$E_{n-1} = (1-\lambda)^{n-2}(E_1 + d_p) + \frac{(1-\lambda) - (1-\lambda)^{n-2}}{\lambda} d_p \tag{9}$$

The energy dissipation rate of the nth baffle can be expressed as follows:

$$\eta_n = \frac{\Delta E}{E_t} = 1 - \frac{E_{n-1}}{E_1 + (n-2)d_p} = 1 - \frac{(1-\lambda)^{n-2}\left(\frac{E_1}{d_p} + 1\right) + \frac{(1-\lambda) - (1-\lambda)^{n-2}}{\lambda}}{\frac{E_1}{d_p} + (n-2)} \tag{10}$$

where ΔE is the energy difference between the second and nth baffle, and E_t is the total energy of the water flow.

Based on Equation (10), the energy dissipation rate of any baffle in the shaft can be obtained as a function of the specific energy of the second baffle E_1, baffle spacing d_p, and energy loss ratio λ. The numerical simulation results show that the specific energy of the second baffle was not only affected by the flow rate but was also related to the baffle spacing and the width of the baffle edge. Hence, the specific energy of the second baffle E_1 could be expressed as follows:

$$E_1 = f(Q^*, d_p, B) \tag{11}$$

Equation (11) can be rewritten in a dimensionless variable as follows:

$$\frac{E_1}{d_p} = f\left(Q^*, \frac{B}{d_p}\right) \tag{12}$$

Based on theoretical analysis, $E_1/d_p \propto Q^*$. Thus, Equation (12) can be formulated as follows:

$$\frac{E_1}{d_p} = a_1 (Q^*)^{b_1} \left(\frac{B}{d_p}\right)^{c_1} \tag{13}$$

where a_1, b_1, and c_1 are unknown parameters, and $b_1 > 0$.

Combined with the numerical simulation results, a mathematical model for E_1, Q^*, d_p, and B was established using a multiple linear regression model, and the fitting formula of the dimensionless specific energy was then obtained:

$$\frac{E_1}{d_p} = 1.483 (Q^*)^{0.669} \left(\frac{B}{d_p}\right)^{1.105} \tag{14}$$

The applicable scope of Equation (14) is $0.075 \le Q^* \le 0.175$. To verify the accuracy of Equation (14), Figure 9 illustrates the comparison result between the calculated and simulated values of the dimensionless specific energy E_1/d_p. It indicates that a good agreement was obtained between the calculated and simulated values, and that Equation (14) allows a direct estimation of the specific energy at the second baffle.

The energy loss ratio λ is defined as follows:

$$\lambda = \frac{(E_{n-2} + d_p) - E_{n-1}}{E_{n-2} + d_p} \tag{15}$$

where E_{n-1} and E_{n-2} are the specific energies of the nth and $(n-1)$th baffle, respectively.

The energy loss ratio λ is related to the baffle spacing d_p and the flow rate Q^*, and d_p/B is defined as the relative drop height of the water flow. Based on the numerical simulation, the fitting formula for the energy loss ratio λ as a function of the relative drop height d_p/B at different flow rates was obtained:

$$\lambda = \begin{cases} 0.272\dfrac{d_p}{B} + 0.484, & (0.075 \le Q^* \le 0.100) \\ 0.387\dfrac{d_p}{B} + 0.360, & (0.100 < Q^* < 0.150) \\ 0.452\dfrac{d_p}{B} + 0.251, & (0.150 \le Q^* \le 0.175) \end{cases} \tag{16}$$

Figure 10 shows the three fit lines of the energy loss ratio λ at different flow rates. The fitting degree of Equation (16) was high, and it is suitable for calculating the energy loss ratio for $0.075 \le Q^* \le 0.175$.

For the energy dissipation of the baffle drop shaft under the free-drop flow regime, the specific energy of the second baffle and energy loss ratio could be obtained by Equations (14) and (16), respectively. These can then be substituted into Equation (10) to calculate the energy dissipation rate on any baffle.

To verify the accuracy of Equation (10), the calculated energy dissipation rate values were plotted against the simulated values. Figure 11 shows a comparison between the calculated and simulated values of the energy dissipation rate under four different conditions. The calculation error was less than 5.7%, which shows that Equation (10) had a better ability to predict the energy dissipation rate of the baffle drop shaft in the free-drop flow regime.

Energy dissipation mechanisms

Energy dissipation types

The discharge process of a baffle drop shaft includes many kinds of flow phenomena, such as hydraulic drops, high-

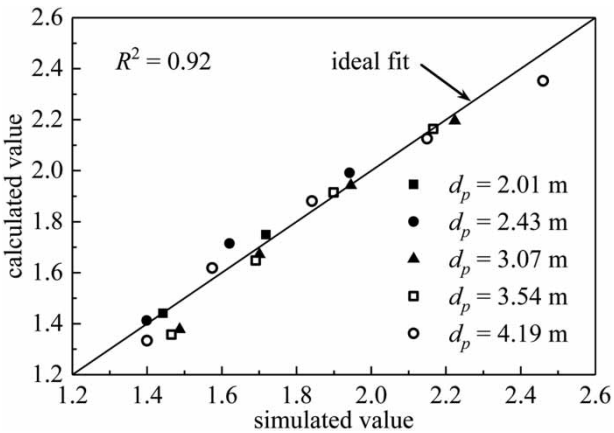

Figure 9 | Comparison of calculated and simulated values of E_1/d_p.

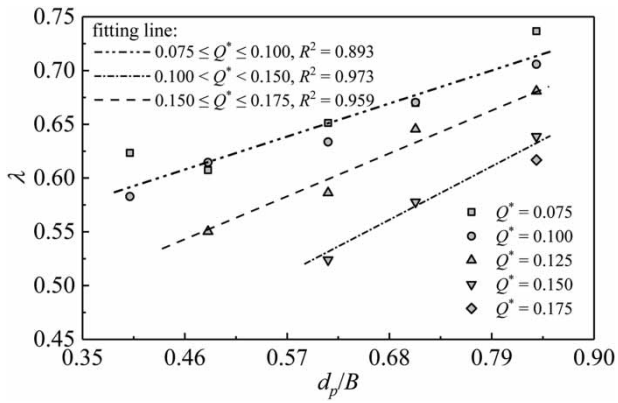

Figure 10 | Fitting lines of λ and d_p/B at different Q^*.

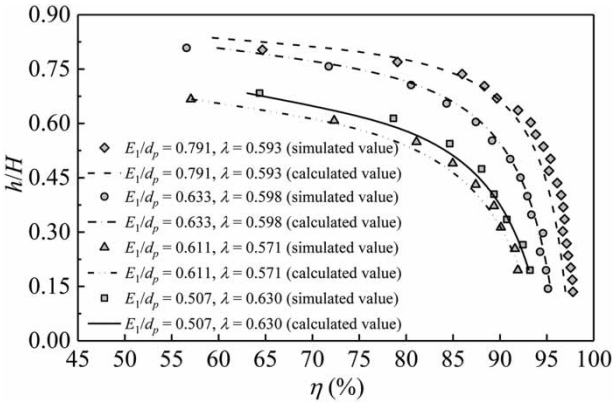

Figure 11 | Comparison of calculated and simulated values of η at different baffles.

speed jets, and oscillating flow. Due to the friction, impingement, breakup, and coalescence of the water flow, the process of energy conversion and dissipation inside the shaft is very complicated. In general, the energy dissipation type in the baffle drop shaft can be divided into the following three categories:

(1) Friction between the water flow and the surfaces of the baffles and shaft walls. Due to the presence of the baffles and shaft walls, the flow boundary could not expand outward during the dropping process, and water flow rubbed against and collided with the shaft structure constantly. This caused the flow velocity to change over a short time and the kinetic energy of the water flow to decrease rapidly.
(2) Breakup and coalescence of the water flow. During the discharge process, the water flows collided and mixed. This included the rolling of impact waves on the baffles, coalescence between the dropping flow and the water cushion, and the breakup and impingement of the plunging flow with reverse flow at the bottom of the shaft. As a result, the gravitational potential energy of the upstream flow was converted into kinetic energy and thermal energy, which was accompanied by energy loss.
(3) Viscosity effect of flow fluid. Viscosity is an inherent property of fluids. The relative motion between the particles in the flow caused the viscous forces to do work on the shear deformation, which led to energy loss.

However, the viscosity of water is small and is generally not considered in engineering fluid mechanics. Therefore, the energy dissipation mechanism of the baffle drop shaft is mainly manifested as friction between the water flow and shaft structure as well as the breakup and coalescence of the water streams.

Energy dissipation modes

Apart from the above division methods, based on the different energy dissipation positions of the baffle drop shaft, the energy dissipation of the water flow could also be divided into the following three modes:

(1) Inlet energy dissipation. At low flow rates ($Q^* \leq 0.125$), the water flow dropped to the first baffle directly after entering the shaft. Some of the water flow fell along the baffle edge to the second baffle, and the rest formed an impact wave near the side of the shaft wall. When the flow rate increased ($0.125 < Q^* \leq 0.250$), the water flow collided head-on with the dividing wall, and the great impact force caused the water to splash. One part of the water flow bounced from the dividing wall and dropped onto the second baffle, and the other part broke over the first baffle and flowed to the second baffle rapidly after the coalescence with the water cushion.
(2) Baffle energy dissipation. When the flow rate was low, the flow regime manifested as free-drop flow. After the water flow fell to the water cushion, water and air were mixed to form strong local turbulence on the baffles. As the flow rate increased, the flow regime began to change from free-drop flow to wall-impact confined flow. In addition to the breakup and coalescence of water on the baffles, an impact wave phenomenon was formed between the shaft wall and water jet. Due to the rolling and impingement, the kinetic energy of the water flow was dissipated continuously. The water cushion and impact wave are shown in Figure 5(f).
(3) Shaft-bottom energy dissipation. At low flow rates, the plunging flow collided with the reverse flow violently at the bottom of the shaft, which was accompanied by energy loss. With the increase in the flow rate, some baffles at the bottom of the shaft were submerged. These baffles extended the flow path of the water and increased the frictional resistance along the shaft bottom. Intermittent vortices were generated under the baffle edge, forming local resistance, and dissipated the energy from the upstream flow.

Taking the drop shaft with $d^* = 0.485$ as an example, the energy difference between the inlet and outlet pipes could be obtained based on the horizontal plane of the outlet pipe axis. The proportions (ω) of the energy dissipation modes at different flow rates were calculated through the numerical simulation results. Figure 12 shows the energy dissipation proportions of different energy dissipation

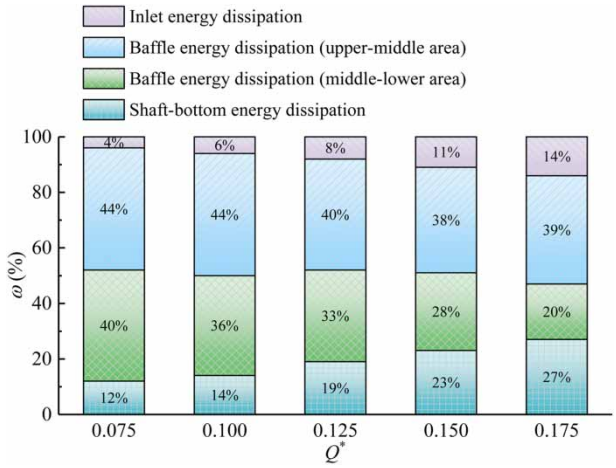

Figure 12 | Proportions of different energy dissipation modes.

modes. The baffles played a major role in the energy dissipation of the drop shaft at low flow rates ($Q^* \leq 0.125$), and the differences in the energy dissipation proportions between the middle-lower and upper-middle areas were small. For large flow rates ($0.125 < Q^* \leq 0.175$), the proportion of inlet energy dissipation increased, but the energy dissipation of the drop shaft was mainly achieved through the baffles and shaft-bottom. The proportions of energy dissipation at middle-lower and upper-middle areas were about 1.4:1 to 2:1, indicating that baffle energy dissipation in the upper-middle area was more prominent at high flow rates.

CONCLUSIONS AND RECOMMENDATIONS

Baffle drop shafts are successfully used in deep tunnel drainage systems to transfer storm water in shallow sewer systems to underground tunnels. However, there have been no systematic studies on the turbulence characteristics and energy dissipation mechanisms of baffle drop shaft structures. To fill this research gap, a 3D numerical model based on the Realizable k-ϵ model and Volume of Fluid (VOF) method was applied, which was validated using 1:25 scale physical model tests. In particular, the influences of different flow rates and baffle spacings on the turbulence characteristics were studied. The main conclusions of this study are as follows.

A baffle spacing that is too dense or too sparse is not conducive to energy dissipation and discharge. The turbulent kinetic energy is more uniformly distributed in the shaft with an increase in the baffle spacing, and the discharge capacity is improved. However, the large baffle spacing increases the hydrodynamic load on the baffles. Therefore, the minimum baffle spacing is the optimal structural design at the design flow rate when the flow regime is free-drop flow.

Based on the basic assumptions and numerical simulation results, a calculation model of the baffle energy dissipation was established. Using fitting formulas of the second baffle specific energy and energy loss ratio, this model could accurately calculate the energy dissipation rates of each baffle in the free-drop flow regime, and the calculation error was less than 5.7%.

The energy dissipation mechanisms of baffle drop shafts were expounded in detail through the energy dissipation types and modes. The energy dissipation mode can be divided into inlet energy dissipation, baffle energy dissipation, and shaft-bottom energy dissipation. The calculations showed that the flow rate affects the proportions of the different energy dissipation modes. Baffles play a major role in the energy dissipation of the drop shaft at low flow rates, but for high flow rates, the energy dissipation is mainly achieved via the baffles and the shaft bottom.

It should be noted that these results were drawn based on simulations and experiments with only steady flow, horizontal baffle, and center dividing wall position. Practically, unsteady flow is more common for baffle drop shafts, and it is necessary to investigate the turbulence characteristics of the shaft under unsteady flow conditions. Moreover, different scale numerical simulations and experiments need to be carried out considering the scale effect.

ACKNOWLEDGEMENTS

We thank LetPub (www.letpub.com) for its linguistic assistance during the preparation of this manuscript. This work was supported by the National Natural Science Foundation of China (Grant No. 51478403).

DATA AVAILABILITY STATEMENT

All relevant data are included in the paper or its Supplementary Information.

REFERENCES

ANSYS Fluent Theory Guide; Release 16.0. 2015 ANSYS Inc., Canonsburg, PA, USA.

Beijing General Municipal Engineering Design and Research Institute Co., Ltd 2017 *Design Manual for the Water Supply and Drainage (2nd edn)/Urban Drainage (vol. 5)*. China Architecture & Building Press, Beijing, China, pp. 26–29.

Camino, G. A., Zhu, D. Z. & Rajaratnam, N. 2011 Hydraulics of stacked drop manholes. *Journal of Irrigation and Drainage Engineering* **137** (8), 537–552.

Chanson, H. 2007 Air entrainment processes in a full-scale rectangular dropshaft at large flows. *Journal of Hydraulic Research* **45** (1), 43–53.

Crispino, G., Pfister, M. & Gisonni, C. 2019 Hydraulic design aspects for supercritical flow in vortex drop shafts. *Urban Water Journal* **16** (3), 225–234.

Crispino, G., Contestabile, P., Vicinanza, D. & Gisonni, C. 2021 Energy head dissipation and flow pressures in vortex drop shafts. *Water* **13** (2), 165.

Gildeh, H. K., Mohammadian, A., Nistor, I. & Qiblawey, H. 2014 Numerical modeling of turbulent buoyant wall jets in stationary ambient water. *Journal of Hydraulic Engineering* **140** (6), 04014012.

Granata, F., Marinis, G. D., Gargano, R. & Hager, W. H. 2011 Hydraulics of circular drop manholes. *Journal of Irrigation and Drainage Engineering* **137** (2), 102–111.

Hnaien, N., Marzouk, S., Aissia, H. B. & Jay, J. 2018 Numerical investigation of velocity ratio effect in combined wall and offset jet flows. *Journal of Hydrodynamics* **30** (6), 1105–1119.

Jiao, F. & Deng, X. H. 2013 Structural optimization of converging-diverging tube based on heat transfer enhancement for self-support rectangle heat exchanger. *CIESC Journal* **64** (7), 2376–2385.

Liao, L., An, R. D., Li, J., Yi, W. M., Liu, X. F., Meng, W. K. & Zhu, L. 2019 Hydraulic characteristics of stepped spillway dropshafts for urban deep tunnel drainage systems: the case study of Chengdu city. *Water Science and Technology* **80** (8), 1538–1548.

Liu, H., Jia, Y. W. & Niu, C. W. 2017 'Sponge city' concept helps solve China's urban water problems. *Environmental Earth Sciences* **76** (14), 473.

Liu, Z. P., Guo, X. L., Xia, Q. F., Fu, H., Wang, T. & Dong, X. L. 2018 Experimental and numerical investigation of flow in a newly developed vortex drop shaft spillway. *Journal of Hydraulic Engineering* **144** (5), 04018014.

Mahmoudi-Rad, M. & Khanjani, M. J. 2019 Energy dissipation of flow in the vortex structure: experimental investigation. *Journal of Pipeline Systems Engineering and Practice* **10** (4), 04019027.

Margevicius, A., Schreiber, A., Switalski, R., Lyons, T., Benton, S. & Glovick, S. 2010 A baffling solution to a complex problem involving sewage drop structures. *Proceedings of the Water Environment Federation* **6**, 1–9.

Mohsin, M. & Kaushal, D. R. 2016 3D CFD validation of invert trap efficiency for sewer solid management using VOF model. *Water Science and Engineering* **9** (2), 106–114.

Odgaard, A. J., Lyons, T. C. & Craig, A. J. 2013 Baffle-drop structure design relationships. *Journal of Hydraulic Engineering* **139** (9), 995–1002.

Pfister, M., Crispino, G., Fuchsmann, T., Ribi, J. & Gisonni, C. 2018 Multiple inflow branches at supercritical-type vortex drop shaft. *Journal of Hydraulic Engineering* **144** (11), 05018008.

Qi, Y. F., Wang, Y. R. & Zhang, J. M. 2018 Three-dimensional turbulence numerical simulation of flow in a stepped dropshaft. *Water* **11**, 30.

Shen, J. Y., Wu, J. H. & Ma, F. 2019 Hydraulic characteristics of stepped spillway dropshafts. *Science China Technological Sciences* **62** (5), 868–874.

Stirrup, M., Margevicius, T., Hrkac, T. & Baca, A. 2012 A baffling solution to sewage conveyance in York Region, Ontario. *Proceedings of the Water Environment Federation* **4**, 74–90.

Wang, X. C., Zhang, J., Fu, Z. F., Xu, H., Xu, T. Y. & Zhou, C. L. 2020 Influences of flow rate and baffle spacing on hydraulic characteristics of a novel baffle dropshaft. *Water Science and Engineering* **13** (3), 233–242.

Wu, H. C., Huang, G. R., Meng, Q. Q., Zhang, M. Z. & Li, L. C. 2016 Deep tunnel for regulating combined sewer overflow pollution and flood disaster: a case study in Guangzhou City, China. *Water* **8**, 329.

Yang, Q. H. & Yang, Q. 2020 Experimental investigation of hydraulic characteristics and energy dissipation in a baffle-drop shaft. *Water Science and Technology* **82** (8), 1603–1613.

Yang, Q., Yang, Q. H., Zheng, L. N., Tian, Q., Liu, Y. Q., Yao, J. T., Yao, Y. & Mu, Y. 2020 Experimental study on discharge and energy dissipation of baffle-drop shaft in deep tunnel drainage system. *Journal of Southwest Jiaotong University* **55** (6), 1247–1256.

Zhang, J. M., Chen, J. G., Xu, W. L., Wang, Y. R. & Li, G. J. 2011 Three-dimensional numerical simulation of aerated flows downstream sudden fall aerator expansion-in a tunnel. *Journal of Hydrodynamics* **23** (1), 71–80.

Zhang, W. C., Wang, J. X., Zhou, C. B., Dong, Z. S. & Zhou, Z. 2018 Numerical simulation of hydraulic characteristics in a vortex drop shaft. *Water* **10**, 1393.

First received 5 January 2021; accepted in revised form 25 March 2021. Available online 7 April 2021